Assessing Angular Momentum, Kinetics, and Energetics of a Rigid Body Using a Single Inertial Measurement Unit

Zhang, Junhao; Muijzer, Frodo; Vallery, Heike; Veltink, Peter H.

DOI
10.1109/JSEN.2023.3341472

Publication date
2024

Document Version
Final published version

Published in
IEEE Sensors Journal

Assessing Angular Momentum, Kinetics, and Energetics of a Rigid Body Using a Single Inertial Measurement Unit

Junhao Zhang, Frodo Muijzer, Heike Vallery, *Member, IEEE*, and Peter H. Veltink, *Senior Member, IEEE*

***Abstract*—Angular momentum, kinetics, and energetics, including total mechanical energy and its rate of change in relation to power exchange, are important quantities when analyzing human motion in sports, physical labor, and rehabilitation. Inertial measurement units (IMU)-based motion capture (MOCAP) systems provide a portable solution for the ambulatory analysis of these quantities which optical MOCAP systems do not offer. Yet, evaluating IMU-based estimates of these quantities by referencing optical systems is limited by the fact that these systems only measure positions, not kinetic and energetic quantities. To evaluate the accuracy of an IMU-based method for estimating kinetic and energetic quantities without using any external reference, firstly, we propose an estimation method only using angular velocity and acceleration signals supplied by an IMU, and apply this to a single rigid body with known mass and inertia. Then, we propose a novel experimental validation method against physical conservation and action/reaction laws that apply during ballistic movements, using a suitably designed and reconfigurable rigid body with a structure of three orthogonal dumb-bells. The results demonstrated that we could estimate the angular momentum, kinetics, and energetics of a rigid body by only using angular velocity and acceleration signals of an IMU, and the estimation accuracy was well evaluated by the proposed validation method. However, the results showed that the errors in original IMU measurements under dynamic conditions especially concerning angular velocity, uncertainties in calculating rigid body parameters, and vibration propagation due to limited rigidity of tubes of the rigid body influenced the estimation accuracy.**

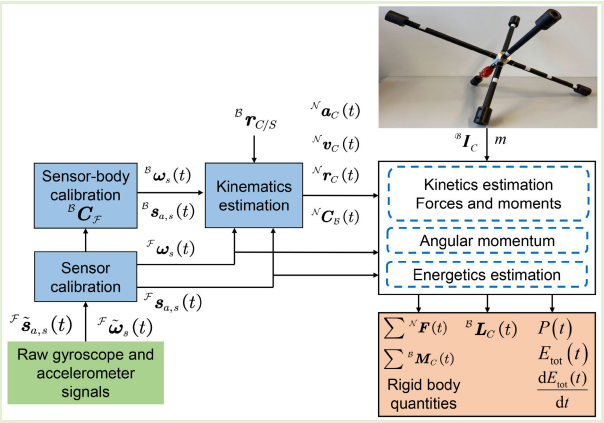

***Index Terms*— Angular momentum, energetics, inertial measurement unit (IMU), kinetics.**

I. Introduction

FOR a better understanding of the biomechanics of human movement, designing safer and more effective assistive devices and promoting optimal recovery from injury or disability, assessment of angular momentum, kinetics, and energetics of the human body is essential. For example, in sports, joint kinetics can be used to analyze the effect of fatigue to suggest methods of reducing injury risk [1], [2]. The assessment of the centroidal angular momentum of the human body and its parts can help understand balance recovery strategies [3] or inspire human-like balance controllers for exoskeletons [4]. Quantitative assessment in energetics such as mechanical energy and power exchange could reveal how humans optimize their mechanical energy absorption/release strategies through their neuromuscular system, which could contribute to the assessment of movement disorder [5] or the development of biped robots [6].

Golden standard estimates of human kinetics and energetics are usually established in a human motion capture (MOCAP) lab, traditionally equipped with an optical motion capture system and force plates [7], which are only performed in structured laboratory environments. In addition, the computation of kinematic quantities such as angular velocity/acceleration and center of mass (CoM) velocity/acceleration from marker posi-

Manuscript received 3 October 2023; accepted 28 November 2023. Date of publication 22 December 2023; date of current version 31 January 2024. This work was supported by China Scholarship Council (CSC) under Grant 202008330287. The associate editor coordinating the review of this article and approving it for publication was Dr. Qammer H. Abbasi. *(Corresponding author: Junhao Zhang.)*

Junhao Zhang, Frodo Muijzer, and Peter H. Veltink are with the Department of Biomedical Signals and Systems, University of Twente, 7522 NB Enschede, The Netherlands (e-mail: j.zhang-7@utwente.nl; f.muijzer@utwente.nl; p.h.veltink@utwente.nl).

Heike Vallery is with the Institute of Automatic Control, RWTH Aachen University, 52074 Aachen, Germany, also with the Department of Biomechanical Engineering, TU Delft, 2628 CD Delft, The Netherlands, and also with the Department of Rehabilitation Medicine, Erasmus MC, 3015 GD Rotterdam, The Netherlands (e-mail: h.vallery@irt.rwth-aachen.de).

Data is available on-line at https://doi.org/10.5281/zenodo.10245528.

Digital Object Identifier 10.1109/JSEN.2023.3341472

tion data requires two successive numerical differentiations. Doing so amplifies errors in position data (due to measurement error, marker occlusion, skin motion, etc.) and thus, resulting in potentially large errors in the kinematic quantities and estimation of human energetics.

Inertial measurement units (IMUs) offer a balanced trade-off among accuracy, cost, and usability, making them widely employed for human motion analysis. IMUs directly capture linear acceleration and angular velocity of the attached rigid body, which are crucial for kinetic and energetic analysis, requiring just one differentiation to yield the angular acceleration. Despite potential drift due to errors in initial IMU measurements, their broad applications in everyday scenarios underscore their efficient and accurate kinematics estimation [8], [9], [10], [11]. Utilizing masses and inertia tensors of individual body segments scaled by a biomechanical model, IMUs extend to estimating human kinetics and energetics. They were used to estimate quantities like ground reaction force (GRF), ground reaction moment (GRM), whole-body concentric power [12], and torso kinetic energy [13], employing biomechanical models [14], [15], [16] or machine learning methods [17], [18]. Notably, these studies in estimating kinetics and energetics all reference the gold standard of optical MOCAP systems, inheriting inaccuracies arising from differentiation errors from marker position data in required kinematics. The accuracy of the marker position data is highly hampered by line-of-sight requirements and processing models, and could potentially lead to large differences between IMU-based and optical MOCAP-based methods. Furthermore, these studies employ the same mass and inertia tensors for both IMU-based and optical MOCAP-based kinetic and energetic estimations, leading to questionable evaluation of the validity of the IMU-based analysis on the kinetic and energetic level, given the errors that exist in estimating the CoM, total mass, or inertia tensor. Additionally, force and moment (F&M) sensors have frequently served as the benchmark for kinetic estimations [19], [20]. However, their utilization increases costs and experimental complexity. The authors are unaware of prior work utilizing a single IMU for estimating the kinetics, angular momentum, and energetic quantities of a rigid body while adequately validating estimation accuracy without external devices like optical MOCAP or force sensors.

From the motivations above, the objective of this article is to present and experimentally validate a concept for estimating the angular momentum, kinetics, and energetics, including total mechanical energy and its rate of change in relation to the power exchange of a single rigid body, using only angular velocity and acceleration signals from IMUs. Our contributions are summarized as follows.

1) We present a complete measurement framework for estimating the kinetics, angular momentum, total mechanical energy and its rate of change, and power exchange for a rigid body based on a single IMU.
2) We design a novel experimental evaluation method to validate the presented IMU-based estimation methods during free ballistic motions based on physical conservation and action/reaction laws in classical mechanics, without using external measurement devices like F&M sensors or optical MOCAP systems as the reference. Using a suitably designed and reconfigurable rigid body with a structure of three orthogonal dumb-bells, instrumented with attached IMUs, we were able to conduct the experiment and analyze the proposed estimation and evaluation concept under varying rigid body mass, structure, and angular momentum conditions.

II. Related Works

Although optical MOCAP systems and force plates have traditionally dominated human motion analysis, several efforts have aimed to create more wearable and everyday-friendly solutions. ForceShoes which were integrated on-board IMUs and 3-D F&M sensors were used to reconstruct foot kinematics and kinetics during walking [21], [22]. However, it is still not practical to use them every day due to the bulky 3-D F&M sensors. Pressure insoles, a lightweight alternative to 3-D F&M sensors [23], often relied on machine learning methods but struggled with accuracy in estimating shear forces and susceptibility to subject variations [24]. Surface electromyography (sEMG) is very useful to measure muscle activation and estimate internal forces or torques [25], [26], [27], but it is not feasible using sEMG to assess other quantities like angular momentum and energetics. In contrast, IMUs can continuously capture whole-body kinematics using measured acceleration, angular rate, and/or magnetic field. Their portability and ability to operate without a clear line of sight make them highly appealing. Initially, van den Bogert et al. [28] used accelerometers alone to estimate the forces and moments of the hip joint. Nowadays, with the development of the sensor technology and algorithms, IMU-based kinematics and GRF & GRM estimations could then be used to assess the inverse dynamics of human segments [29], [30]. Based on the estimated kinematics and kinetics of the human body, various quantities, including power transfer between the body and environment [19] and torso kinetic energy [31], can be derived. Recognizing these advantages, this article employed IMUs to estimate the kinetics and energetics of a single rigid body.

III. Methods

Here, the methods used to estimate and evaluate the targeted quantities of a single rigid body are further explained, which are kinetics, angular momentum, energetics including the total mechanical energy and its rate of change, and power exchange. First, the mathematical foundations for estimating the targeted quantities from original IMU signals are described. Then, the measurement system and a novel experimental validation method are introduced, followed by the experimental protocol and analysis of results.

A. Mathematical Foundations

1) Definitions and Kinematics: Three coordinate systems (CS) were used as presented in Fig. 1(a), the kinematic diagram of the rigid body with the implemented IMU. They include inertial CS, body CS, and sensor CS. Their origins

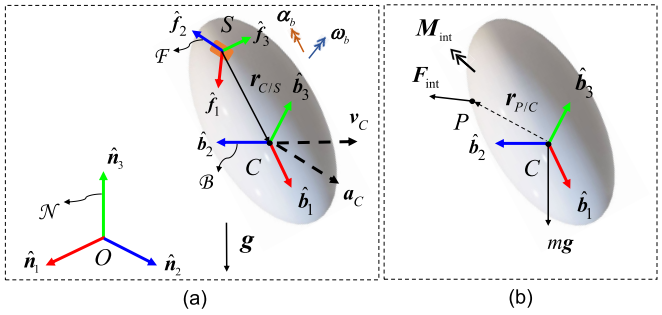

Fig. 1. (a) Kinematic diagram of the rigid body with the implemented IMU, (b) FBD of the rigid body. $\boldsymbol{F}_{\text{int}}$ and $\boldsymbol{M}_{\text{int}}$ are the interaction F&M between the rigid body and external environment. The meaning of the indicated quantities is given in the main text of the article.

are O on the ground, CoM C, and a known sensor location S, respectively. Their axis directions are defined by right-handed triads of orthogonal unit vectors $\mathcal{N} = \{\hat{\boldsymbol{n}}_1, \hat{\boldsymbol{n}}_2, \hat{\boldsymbol{n}}_3\}$, $\mathcal{F} = \{\hat{\boldsymbol{f}}_1, \hat{\boldsymbol{f}}_2, \hat{\boldsymbol{f}}_3\}$, $\mathcal{B} = \{\hat{\boldsymbol{b}}_1, \hat{\boldsymbol{b}}_2, \hat{\boldsymbol{b}}_3\}$, respectively. In contrast to a coordinate system, a triad only describes orientations, no absolution location in space [32]. The relative position vector ${}^{\mathcal{B}}\boldsymbol{r}_{C/S}$ of the CoM C with respect to the sensor location S is a fixed vector in the body triad which can be determined in advance. The raw gyroscope and accelerometer measurements (including gravity) of the IMU are defined and expressed in the sensor triad $\mathcal{F}$ as ${}^{\mathcal{F}}\tilde{\boldsymbol{\omega}}_s(t)$ and ${}^{\mathcal{F}}\tilde{\boldsymbol{s}}_{a,s}(t)$, respectively. In this article, subscripts "s" and "b" refer to the sensor and body for any signal.

To increase the estimation accuracy, the low-cost IMU was firstly manually calibrated using the method proposed in [33] to correct the scale factors, biases, and sensor axis misalignments. The calibrated measurements ${}^{\mathcal{F}}\boldsymbol{\omega}_s(t)$ and ${}^{\mathcal{F}}\boldsymbol{s}_{a,s}(t)$ were then transferred to the body CS by pre-multiplying the constant rotation matrix ${}^{\mathcal{B}}\boldsymbol{C}_{\mathcal{F}}$ which can be calculated in advance, that is,

$$\begin{aligned} {}^{\mathcal{B}}\boldsymbol{\omega}_s(t) &= {}^{\mathcal{B}}\boldsymbol{C}_{\mathcal{F}}\,{}^{\mathcal{F}}\boldsymbol{\omega}_s(t) \\ {}^{\mathcal{B}}\boldsymbol{s}_{a,s}(t) &= {}^{\mathcal{B}}\boldsymbol{C}_{\mathcal{F}}\,{}^{\mathcal{F}}\boldsymbol{s}_{a,s}(t). \end{aligned} \tag{1}$$

${}^{\mathcal{B}}\boldsymbol{\omega}_s(t)$ and ${}^{\mathcal{B}}\boldsymbol{s}_{a,s}(t)$ were used to calculate the orientation ${}^{\mathcal{N}}\boldsymbol{C}_{\mathcal{B}}(t)$, which is further introduced in Appendix A. ${}^{\mathcal{B}}\boldsymbol{s}_{a,s}(t)$ is the total acceleration measurements of the IMU expressed in body triad and its relationship with the free acceleration of the IMU ${}^{\mathcal{N}}\boldsymbol{a}_s(t)$ and gravity ${}^{\mathcal{N}}\boldsymbol{g}$ is

$${}^{\mathcal{B}}\boldsymbol{s}_{a,s}(t) = {}^{\mathcal{N}}\boldsymbol{C}_{\mathcal{B}}(t)^{\mathrm{T}}\big({}^{\mathcal{N}}\boldsymbol{a}_s(t) - {}^{\mathcal{N}}\boldsymbol{g}\big). \tag{2}$$

The angular acceleration was calculated by numerically differentiating the angular velocity measured by the IMU, to approximate ${}^{\mathcal{B}}\boldsymbol{\alpha}_s(t) = {}^{\mathcal{B}}\boldsymbol{C}_{\mathcal{F}}\,{}^{\mathcal{F}}\dot{\boldsymbol{\omega}}_s(t)$. During offline data processing, a second-order (biquad) zero-phase low-pass Butterworth filter using the MATLAB function *filtfilt*() was applied to reduce the high-frequency noises due to the numerical differentiation. As a part of the kinematics estimation, the angular velocity/acceleration of the rigid body are

$$\begin{aligned} {}^{\mathcal{B}}\boldsymbol{\omega}_b(t) &= {}^{\mathcal{B}}\boldsymbol{\omega}_s(t) \\ {}^{\mathcal{B}}\boldsymbol{\alpha}_b(t) &= {}^{\mathcal{B}}\boldsymbol{\alpha}_s(t) = {}^{\mathcal{B}}\boldsymbol{C}_{\mathcal{F}}\,{}^{\mathcal{F}}\dot{\boldsymbol{\omega}}_s(t). \end{aligned} \tag{3}$$

Algorithm 1 Inertial Sensing Method

Input: ${}^{\mathcal{B}}\boldsymbol{C}_{\mathcal{F}}$, ${}^{\mathcal{B}}\boldsymbol{r}_{C/S}$, raw IMU measurements ${}^{\mathcal{F}}\tilde{\boldsymbol{\omega}}_s(t)$ and ${}^{\mathcal{F}}\tilde{\boldsymbol{s}}_{a,s}(t)$

Output: The targeted quantities ${}^{\mathcal{B}}\boldsymbol{L}_C(t)$, $\sum {}^{\mathcal{N}}\boldsymbol{F}(t)$, $\sum {}^{\mathcal{B}}\boldsymbol{M}_C(t)$, $E_{\text{tot}}(t)$, $\frac{\mathrm{d}E_{\text{tot}}(t)}{\mathrm{d}t}$, and $P(t)$.

1: Calibrate the raw measurements → ${}^{\mathcal{F}}\boldsymbol{\omega}_s(t)$ and ${}^{\mathcal{F}}\boldsymbol{s}_{a,s}(t)$;
2: Transfer the measurements to body triad by ${}^{\mathcal{B}}\boldsymbol{C}_{\mathcal{F}}$ → ${}^{\mathcal{B}}\boldsymbol{\omega}_s(t)$ and ${}^{\mathcal{B}}\boldsymbol{s}_{a,s}(t)$;
3: Compute the orientation ${}^{\mathcal{N}}\boldsymbol{C}_{\mathcal{B}}(t)$ as explained in Appendix A;
4: Compute the CoM acceleration ${}^{\mathcal{N}}\boldsymbol{a}_C(t)$, velocity ${}^{\mathcal{N}}\boldsymbol{v}_C(t)$, and position ${}^{\mathcal{N}}\boldsymbol{r}_C(t)$ by (29)-(31), respectively;
5: Estimation of kinetics: Compute the angular momentum ${}^{\mathcal{B}}\boldsymbol{L}_C(t)$, the net force $\sum {}^{\mathcal{N}}\boldsymbol{F}(t)$, and the sum of moments with respect to the CoM $\sum {}^{\mathcal{B}}\boldsymbol{M}_C(t)$ by (8)-(10), respectively;
6: Estimation of energetics: Compute the total mechanical energy $E_{\text{tot}}(t)$ and its time rate of change $\frac{\mathrm{d}E_{\text{tot}}(t)}{\mathrm{d}t}$, and the power exchange $P(t)$ by (15), (16), and (22), respectively. Set $t = t + 1$ and go back to step 1.

After we know the free acceleration of the IMU ${}^{\mathcal{N}}\boldsymbol{a}_s(t)$, orientation ${}^{\mathcal{N}}\boldsymbol{C}_{\mathcal{B}}(t)$ and the angular velocity/acceleration of the rigid body, the estimation of the acceleration of the CoM ${}^{\mathcal{N}}\boldsymbol{a}_{C/O}(t)$ with respect to O can be calculated by the acceleration two point theorem of the rigid body [34], which is introduced in Appendix B. The estimation methods of the position and velocity of the CoM with respect to O, ${}^{\mathcal{N}}\boldsymbol{v}_{C/O}(t)$ and ${}^{\mathcal{N}}\boldsymbol{r}_{C/O}(t)$ are further explained in Appendix C. In case of simplification, we used the following shorthand notations in our article:

$$\begin{aligned} {}^{\mathcal{N}}\boldsymbol{a}_C(t) &:= {}^{\mathcal{N}}\boldsymbol{a}_{C/O}(t), \quad {}^{\mathcal{N}}\boldsymbol{v}_C(t) := {}^{\mathcal{N}}\boldsymbol{v}_{C/O}(t) \\ {}^{\mathcal{N}}\boldsymbol{r}_C(t) &:= {}^{\mathcal{N}}\boldsymbol{r}_{C/O}(t). \end{aligned} \tag{4}$$

The targeted quantities include the angular momentum ${}^{\mathcal{B}}\boldsymbol{L}_C(t)$, the net force $\sum {}^{\mathcal{N}}\boldsymbol{F}(t)$, and the sum of moments acting on the rigid body with respect to its CoM $\sum {}^{\mathcal{B}}\boldsymbol{M}_C(t)$, the total mechanical energy $E_{\text{tot}}(t)$, which includes gravitational potential and kinetic energy, and its time rate of change $((\mathrm{d}E_{\text{tot}}(t))/\mathrm{d}t)$, and the power exchange $P(t)$. **Algorithm 1** and the abstract figure show the steps of the overall inertial sensing method, which will be detailed in the following sections.

2) Estimation of Kinetics: After the kinematics of the rigid body is estimated from IMU measurements, the angular momentum with respect to the body CS is defined as

$${}^{\mathcal{B}}\boldsymbol{L}_C(t) = {}^{\mathcal{B}}\mathbf{I}_C\,{}^{\mathcal{B}}\boldsymbol{\omega}_b(t). \tag{5}$$

The net force and the sum of moments with respect to CoM as shown in Fig. 1(b) are expressed as

$$\sum {}^{\mathcal{N}}\boldsymbol{F}(t) = {}^{\mathcal{N}}\boldsymbol{F}_{\text{int}}(t) + m\,{}^{\mathcal{N}}\boldsymbol{g} = m\,{}^{\mathcal{N}}\boldsymbol{a}_C(t), \tag{6}$$

$$\begin{aligned} \sum {}^{\mathcal{B}}\boldsymbol{M}_C(t) &= {}^{\mathcal{B}}\boldsymbol{M}_{\text{int}}(t) + {}^{\mathcal{B}}\boldsymbol{r}_{P/C} \times \big({}^{\mathcal{N}}\boldsymbol{C}_{\mathcal{B}}(t)^{\mathrm{T}}\,{}^{\mathcal{N}}\boldsymbol{F}_{\text{int}}(t)\big) \\ &= {}^{\mathcal{B}}\mathbf{I}_C\,{}^{\mathcal{B}}\boldsymbol{\alpha}_b(t) + {}^{\mathcal{B}}\boldsymbol{\omega}_b(t) \times {}^{\mathcal{B}}\boldsymbol{L}_C(t). \end{aligned} \tag{7}$$

According to the Newton-Euler equations of motion for a rigid body, where ${}^{\mathcal{B}}\mathbf{I}_C$ is a constant inertia tensor of the rigid body with respect to the CoM expressed in triad $\mathcal{B}$.

Remark 1: By substituting original IMU signals into (5)–(7), ${}^{\mathcal{B}}\boldsymbol{L}_C(t)$, $\sum {}^{\mathcal{N}}\boldsymbol{F}(t)$, and $\sum {}^{\mathcal{B}}\boldsymbol{M}_C(t)$ can be directly related to the measured IMU signals in a computationally efficient way

$$ {}^{\mathcal{B}}\boldsymbol{L}_C(t) = {}^{\mathcal{B}}\boldsymbol{C}_{\mathcal{F}}\left({}^{\mathcal{F}}\mathbf{I}_C\,{}^{\mathcal{F}}\boldsymbol{\omega}_s(t)\right) \tag{8} $$

$$ \begin{aligned} \sum {}^{\mathcal{N}}\boldsymbol{F}(t) = m\,{}^{\mathcal{N}}\boldsymbol{C}_{\mathcal{B}}(t)\,{}^{\mathcal{B}}\boldsymbol{C}_{\mathcal{F}}\big[&{}^{\mathcal{F}}\boldsymbol{s}_{a,s}(t) + {}^{\mathcal{F}}\dot{\boldsymbol{\omega}}_s(t) \times {}^{\mathcal{F}}\boldsymbol{r}_{C/S} \\ &+ {}^{\mathcal{F}}\boldsymbol{\omega}_s(t) \times \left({}^{\mathcal{F}}\boldsymbol{\omega}_s(t) \times {}^{\mathcal{F}}\boldsymbol{r}_{C/S}\right)\big] \\ &+ m\,{}^{\mathcal{N}}\boldsymbol{g} \end{aligned} \tag{9} $$

$$ \sum {}^{\mathcal{B}}M_C(t) = {}^{\mathcal{B}}\boldsymbol{C}_{\mathcal{F}}\big[{}^{\mathcal{F}}\mathbf{I}_C\,{}^{\mathcal{F}}\dot{\boldsymbol{\omega}}_s(t) + {}^{\mathcal{F}}\boldsymbol{\omega}_s(t) \times ({}^{\mathcal{F}}\mathbf{I}_C\,{}^{\mathcal{F}}\boldsymbol{\omega}_s(t))\big] \tag{10} $$

where

$$ {}^{\mathcal{F}}\mathbf{I}_C = {}^{\mathcal{B}}\boldsymbol{C}_{\mathcal{F}}{}^{\mathrm{T}}\,{}^{\mathcal{B}}\mathbf{I}_C\,{}^{\mathcal{B}}\boldsymbol{C}_{\mathcal{F}} \tag{11} $$

$$ {}^{\mathcal{F}}\boldsymbol{r}_{C/S} = {}^{\mathcal{B}}\boldsymbol{C}_{\mathcal{F}}{}^{\mathrm{T}}\,{}^{\mathcal{B}}\boldsymbol{r}_{C/S}. \tag{12} $$

3) Estimation of Energetics: The total mechanical energy $E_{\mathrm{tot}}(t)$ comprises the kinetic energy T and gravitational potential energy V, where

$$ T = \frac{1}{2}m\left\|{}^{\mathcal{N}}\boldsymbol{v}_C(t)\right\|^2 + \frac{1}{2}{}^{\mathcal{B}}\boldsymbol{\omega}_b(t)^{\mathrm{T}}\,{}^{\mathcal{B}}\mathbf{I}_C\,{}^{\mathcal{B}}\boldsymbol{\omega}_b(t) \tag{13} $$

$$ V = -m\,{}^{\mathcal{N}}\boldsymbol{g}^{\mathrm{T}}\,{}^{\mathcal{N}}\boldsymbol{r}_C(t) \tag{14} $$

$$ E_{\mathrm{tot}}(t) = T + V. \tag{15} $$

Taking the first-time derivative of the total mechanical energy yields its time rate of change $((\mathrm{d}E_{\mathrm{tot}}(t))/\mathrm{d}t)$, and by substituting original IMU signals, $((\mathrm{d}E_{\mathrm{tot}}(t))/\mathrm{d}t)$ can be directly related to the measured IMU signals, as shown in (16), bottom of the next page.

The power exchange $P(t)$ between the rigid body and the external environment is

$$ P(t) = P_{F_{\mathrm{int}}}(t) + P_G(t) + P_{M_{\mathrm{int}}}(t) \tag{17} $$

where

$$ \begin{aligned} P_{F_{\mathrm{int}}}(t) &= {}^{\mathcal{N}}\boldsymbol{F}_{\mathrm{int}}(t)^{\mathrm{T}}\,{}^{\mathcal{N}}\boldsymbol{v}_P(t) \\ &= m\left({}^{\mathcal{N}}\boldsymbol{a}_C(t) - {}^{\mathcal{N}}\boldsymbol{g}\right)^{\mathrm{T}}\,{}^{\mathcal{N}}\boldsymbol{v}_P(t) \end{aligned} \tag{18} $$

$$ P_G(t) = m\,{}^{\mathcal{N}}\boldsymbol{g}^{\mathrm{T}}\,{}^{\mathcal{N}}\boldsymbol{v}_C(t) \tag{19} $$

$$ \begin{aligned} P_{M_{\mathrm{int}}}(t) &= {}^{\mathcal{B}}\boldsymbol{M}_{\mathrm{int}}(t)^{\mathrm{T}}\,{}^{\mathcal{B}}\boldsymbol{\omega}_b(t) \\ &= \big[{}^{\mathcal{B}}\mathbf{I}_C\,{}^{\mathcal{B}}\boldsymbol{\alpha}_b(t) + {}^{\mathcal{B}}\boldsymbol{\omega}_b(t) \times {}^{\mathcal{B}}\boldsymbol{L}_C(t) \\ &\quad - {}^{\mathcal{B}}\boldsymbol{r}_{P/C} \times \left({}^{\mathcal{N}}\boldsymbol{C}_{\mathcal{B}}(t)^{\mathrm{T}}\,{}^{\mathcal{N}}\boldsymbol{F}_{\mathrm{int}}(t)\right)\big]^{\mathrm{T}}\,{}^{\mathcal{B}}\boldsymbol{\omega}_b(t). \end{aligned} \tag{20} $$

Since the change in total mechanical energy (including gravitational potential energy) equals the sum of the work of the interaction F&M between the rigid body and external environment, namely, the time rate of change equals the power of the interaction F&M, which is

$$ \frac{\mathrm{d}E_{\mathrm{tot}}(t)}{\mathrm{d}t} = P_{F_{\mathrm{int}}}(t) + P_{M_{\mathrm{int}}}(t). \tag{21} $$

Therefore, the power exchange $P(t)$ between the rigid body and the external environment can be expressed as

$$ P(t) = \frac{\mathrm{d}E_{\mathrm{tot}}(t)}{\mathrm{d}t} + P_G(t). \tag{22} $$

By substituting original IMU signals, we can also directly relate $P(t)$ to measured IMU signals. This formula is omitted here, one can easily get it from (14) to (17).

B. Measurement System

The feasibility of using attached IMUs to estimate the kinetics, angular momentum, total mechanical energy and its rate of change and power exchange of a single rigid body was tested experimentally using a suitably designed and reconfigurable rigid body, which is shown in Fig. 2. It has a symmetrical structure of six light hollow carbon tubes with carbon steel hollow cylinders as masses at the ends of the tubes. The masses of the tubes could be ignored relative to the masses of the hollow cylinders. In the middle, there is an Aluminum disk for fixating the tubes, of which the mass was taken into account. The designed rigid body has a structured shape with angles between tubes 90°, making it easy to calculate the CoM and inertia tensor. Furthermore, the total mass can be changed by changing the end hollow cylinders with different masses. The inertia tensor can also be easily changed by either changing the end hollow cylinders with different masses or changing the structure by removing some of the tubes to create nonsymmetrical rigid bodies.

Two IMUs (MPU-9250, InvenSense Inc.) were implemented in tubes 3 and 5 on the rigid body as shown in Fig. 2. The ranges of the accelerometer and angular velocity sensor were ±16 g and ±2000°/s, respectively. These two IMUs were fixated inside the tubes closely near the cylinder. MATLAB was used to read the data from the IMUs wirelessly at a sampling rate of 100 Hz. The definition of the CS is shown in Fig. 2, including the inertial CS, sensor CS, and body CS.

C. Validation Methods

Without using external reference measurement devices that measure different quantities like the optical MOCAP systems or F&M sensors, we chose to validate the estimation concept of kinetic and energetic quantities shown in **Algorithm 1** based on measurements of the attached IMUs against physical conservation and action/reaction laws in classical mechanics, during ballistic movements.

1) Validation Method Based on Conservation Laws: During free ballistic motions, the angular momentum and total mechanical energy of the whole rigid body keep constant according to the conservation laws of the angular momentum and the total mechanical energy, which further tells that the rate of change of the total mechanical energy of the whole rigid body is zero. The accuracies of the IMU-based estimation methods for the angular momentum, the total mechanical, and its rate of change were verified by evaluating whether these estimated quantities obeyed conservation laws. Based on the attached IMU measurements, the angular momentum of the whole rigid body was estimated by (8) and transferred

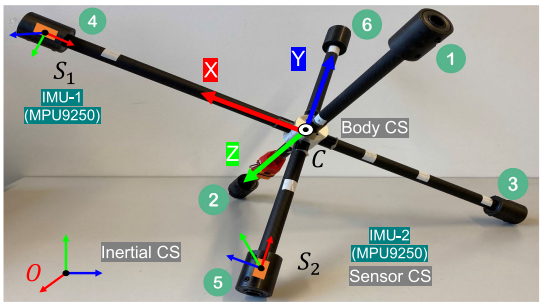

Fig. 2. Self-designed rigid body, IMUs placements and definition of coordinates systems, the length of each tube is listed in Table I. The CoM C was located at the middle point of the disk when the rigid body was symmetrical. In the case of nonsymmetrical structure and masses, CoM was calculated using the definition of CoM from the parameters listed in Table I. S_1 and S_2 were sensor locations.

to the inertial triad $\mathcal{N}$ by pre-multiplying the estimated orientation ${}^{\mathcal{N}}\boldsymbol{C}_{\mathcal{B}}(t)$ since the conservation law of the angular momentum should be designated in an inertial coordinate system, and the total mechanical energy and its rate of change were estimated by (15) and (16), respectively.

2) Validation Method Based on Internal Action/Reaction Laws: Since no external reference measurement devices were used, the net force, the sum of moments with respect to the CoM, and the power exchange between the rigid body cannot be measured as a reference. Instead, we used Newton's third law to evaluate the estimation of force, moment, and power exchange. According to Newton's third law, action/reaction forces and moments between two objects are opposite in direction and equal in magnitude, and the power exchanged between those two objects should also have opposite values with the same magnitude. By dividing the rigid body into two parts as shown in Fig. 3, each with a separate IMU, the action/reaction forces and moments, and the power exchanged between both parts were estimated based on the measurements from their own IMUs. The estimation accuracies of IMU-based estimation methods of the kinetics and power exchange were partially verified by evaluating whether these estimated quantities of two parts were opposite in direction and equal in magnitude. Multiple division methods into parts 1 and 2 for each rigid body were.

1) *Division 1:* part 2 included cylinder 5, part 1 included other cylinders and the middle disk.
2) *Division 2:* part 2 included cylinders 3 and 5, part 1 included other cylinders and the middle disk.
3) *Division 3:* part 2 included cylinders 1, 3, and 5, part 1 included other cylinders and the middle disk.

Fig. 4 showed an example of the division method 2.

During free ballistic motions, the action and reaction forces for parts 1 and 2 can be easily calculated by extracting

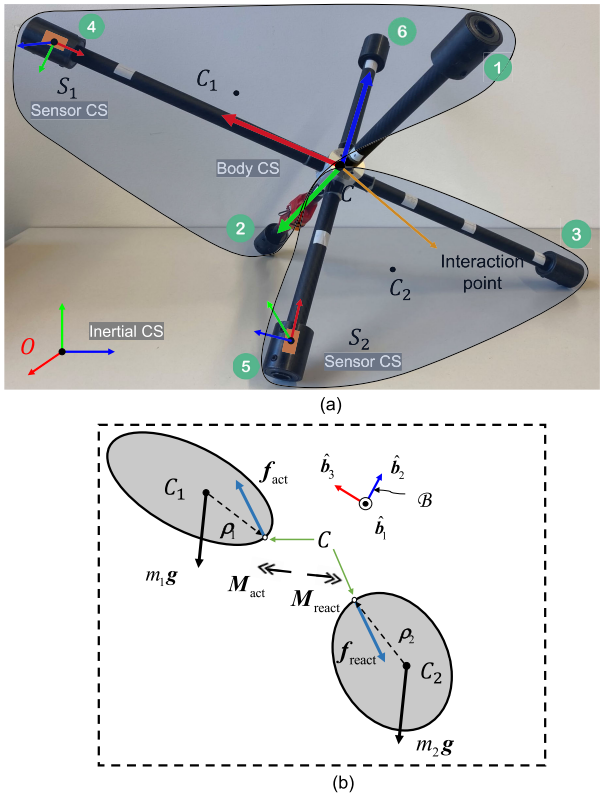

Fig. 3. (a) Division method 2 of the rigid body. Part 2 includes masses 3 and 5, and Part 1 includes other mass elements and the middle disk. (b) FBD of (a).

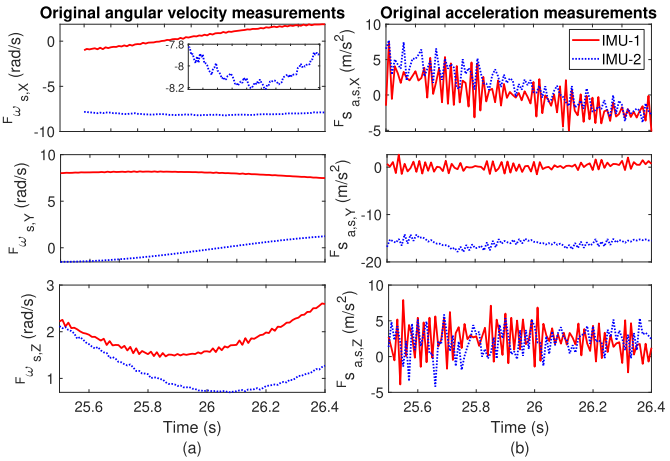

Fig. 4. Original IMU measurements before filtering expressed in the three axes of the sensor triad of the two IMUs, which were taken from a trial of rigid body 1 with a symmetrical structure and a small mass, (a) gyroscope measurements and (b) accelerometer measurements.

gravities from their net forces, which were

$$
\begin{aligned}
{}^{\mathcal{N}}\boldsymbol{f}_{\text{act}}(t) &= \sum {}^{\mathcal{N}}\boldsymbol{F}_1(t) - m_1 {}^{\mathcal{N}}\boldsymbol{g} \\
{}^{\mathcal{N}}\boldsymbol{f}_{\text{react}}(t) &= \sum {}^{\mathcal{N}}\boldsymbol{F}_2(t) - m_2 {}^{\mathcal{N}}\boldsymbol{g}
\end{aligned} \tag{23}
$$

$$
\begin{aligned}
\frac{\mathrm{d}E_{\text{tot}}(t)}{\mathrm{d}t} = m\Big\{ & {}^{\mathcal{N}}\boldsymbol{C}_{\mathcal{B}}(t) {}^{\mathcal{B}}\boldsymbol{C}_{\mathcal{F}} \big[{}^{\mathcal{F}}\boldsymbol{s}_{a,s}(t) + {}^{\mathcal{F}}\dot{\boldsymbol{\omega}}_s(t) \times {}^{\mathcal{F}}\boldsymbol{r}_{C/S} + {}^{\mathcal{F}}\boldsymbol{\omega}_s(t) \times \big({}^{\mathcal{F}}\boldsymbol{\omega}_s(t) \times {}^{\mathcal{F}}\boldsymbol{r}_{C/S} \big) \big] \Big\}^{\mathrm{T}} {}^{\mathcal{N}}\boldsymbol{v}_C(t) \\
& + \big[{}^{\mathcal{F}}\mathbf{I}_C {}^{\mathcal{F}}\dot{\boldsymbol{\omega}}_s(t) + {}^{\mathcal{F}}\boldsymbol{\omega}_s(t) \times \big({}^{\mathcal{F}}\mathbf{I}_C {}^{\mathcal{F}}\boldsymbol{\omega}_s(t) \big) \big]^{\mathrm{T}} {}^{\mathcal{F}}\boldsymbol{\omega}_s(t)
\end{aligned} \tag{16}
$$

TABLE I
LIST OF DIFFERENT SIZES OF RIGID BODIES

	Tube 1 (25cm)	Tube 2 (25cm)	Tube 3 (35cm)	Tube 4 (35cm)	Tube 5 (25cm)	Tube 6 (25cm)	Total mass[1] (kg)	Inertia tensor $(\mathrm{kg}\cdot\mathrm{m}^2)$
Rigid body 1	Cylinder-1	Cylinder-1	Cylinder-1	Cylinder-1	Cylinder-1	Cylinder-1	1.296	$I_{xx}=0.0359$ $I_{yy}=0.0763$ $I_{zz}=0.0607$
Rigid body 2	Cylinder-2	Cylinder-2	Cylinder-2	Cylinder-2	Cylinder-2	Cylinder-2	2.34	$I_{xx}=0.0667$ $I_{yy}=0.1409$ $I_{zz}=0.1124$
Rigid body 3	Cylinder-3	Cylinder-1	Cylinder-1	Cylinder-1	Cylinder-1	Cylinder-1	2.265	$I_{xx}=0.0879$ $I_{yy}=0.1134$ $I_{zz}=0.076$
Rigid body 4	Cylinder-3	Cylinder-1	×	Cylinder-1	×	Cylinder-1	1.889	$I_{xx}=0.0503$, $I_{xy}=0.0015$ $I_{yy}=0.0763$, $I_{xz}=0.0036$ $I_{zz}=0.0607$, $I_{yz}=0.0055$

[1] The masses of cylinder-1, cylinder-2, cylinder-3 and Aluminium disc are 0.188 kg, 0.362 kg, 1.157 kg and 0.168 kg, respectively.

where $\sum {}^{\mathcal{N}}\boldsymbol{F}_1(t)$ and $\sum {}^{\mathcal{N}}\boldsymbol{F}_2(t)$ were their net forces estimated from (9), m_1 and m_2 were the masses of these two parts. As shown in the free body diagram (FBD) of divided parts, their action/reaction moments can be calculated by extracting the moments generated by the action/reaction forces from their sum of moments with respect to their CoMs, which were

$$\begin{aligned} {}^{\mathcal{B}}\boldsymbol{M}_{\text{act}}(t) &= \sum {}^{\mathcal{B}}\boldsymbol{M}_{C_1}(t) - {}^{\mathcal{B}}\boldsymbol{\rho}_1 \times \left({}^{\mathcal{N}}\boldsymbol{C}_{\mathcal{B}}(t)^{\mathrm{T}\mathcal{N}}\boldsymbol{f}_{\text{act}}(t)\right) \\ {}^{\mathcal{B}}\boldsymbol{M}_{\text{react}}(t) &= \sum {}^{\mathcal{B}}\boldsymbol{M}_{C_2}(t) - {}^{\mathcal{B}}\boldsymbol{\rho}_2 \times \left({}^{\mathcal{N}}\boldsymbol{C}_{\mathcal{B}}(t)^{\mathrm{T}\mathcal{N}}\boldsymbol{f}_{\text{react}}(t)\right). \end{aligned} \tag{24}$$

Their sum of moments, $\sum {}^{\mathcal{B}}\boldsymbol{M}_{C_1}(t)$ and $\sum {}^{\mathcal{B}}\boldsymbol{M}_{C_2}(t)$, were estimated from equation (10) respectively for parts 1 and 2. In our case, the interaction point for determining the moment arms $\boldsymbol{\rho}_1$ and $\boldsymbol{\rho}_2$ was assumed to locate at CoM of the whole rigid body, which was shown in Fig. 3(a), thus the moment arms could be determined in advance. Furthermore, based on the FBD in Fig. 3(b), the powers exchanged between both parts were

$$\begin{aligned} P_1(t) &= {}^{\mathcal{N}}\boldsymbol{f}_{\text{act}}(t)^{\mathrm{T}\mathcal{N}}\boldsymbol{v}_C(t) + {}^{\mathcal{B}}\boldsymbol{M}_{\text{act}}(t)^{\mathrm{T}}{}^{\mathcal{B}}\boldsymbol{\omega}_1(t) \\ P_2(t) &= {}^{\mathcal{N}}\boldsymbol{f}_{\text{react}}(t)^{\mathrm{T}\mathcal{N}}\boldsymbol{v}_C(t) + {}^{\mathcal{B}}\boldsymbol{M}_{\text{react}}(t)^{\mathrm{T}}{}^{\mathcal{B}}\boldsymbol{\omega}_2(t) \end{aligned} \tag{25}$$

where ${}^{\mathcal{B}}\boldsymbol{\omega}_1(t)$ and ${}^{\mathcal{B}}\boldsymbol{\omega}_2(t)$ were their angular velocities.

D. Experimental Protocol

Four rigid bodies were included in the experiment as listed in Table I, rigid bodies 1 and 2 had a symmetrical structure with different masses, and rigid bodies 3 and 4 had non-symmetrical structures by replacing a cylinder with a heavier one (rigid body 3) and taking away some cylinders (rigid body 4). The experimental protocol consisted of throwing rigid bodies 1–4 in the air with varying initial angular velocities, each repeated seven trials. The throwing height was around 3 m, and the period of time in the air was around 1 s. To protect the rigid body and the floor, an Aluminum cubical frame with a net was used to catch the rigid body. During each trial, the throwing and airborne phases were preceded and followed by a period of 30 s in which the rigid body was positioned without motion on the ground for 30 s while data collection continued. All data collected with IMUs were saved to be processed later.

E. Data Pre-Processing

MATLAB 2021b was used for data processing, MATLAB function *filtfilt*() was used for filtering. A second-order (biquad) zero-phase low-pass Butterworth filter with cut off frequency of 20 Hz was applied to filter noise from the calibrated gyroscope and accelerometer measurements. The angular acceleration was filtered by a second-order (biquad) zero-phase low-pass Butterworth filter with cut off frequency of 20 Hz. The acceleration estimated by (29) was also smoothed by a second-order (biquad) zero-phase low-pass Butterworth filter with cut off frequency of 20 Hz for further velocity estimation. Then, a second-order (biquad) zero-phase high-pass Butterworth filter was applied to remove the drift in the estimated velocity. After a preliminary analysis, a suitable cut off frequency of 0.5 Hz was set manually. Only the data within the period in the air was used for comparison.

F. Analysis of Results

1) Evaluation Metrics for Angular Momentum Conditions: First, the median values of the modulus and angles between the estimated whole-body angular momentum and *X*/*Y* axes of the inertial triad over seven trials of each body were calculated. Subsequently, the minimum, first quartile, median, third quartile, and a maximum of these median values were compared. Relatively larger Max-min range and interquartile range (IQR) of the median values represented extensively varying angular momentum conditions, compared with the median values.

2) Evaluation Metrics Based on Conservation Laws: Then, the accuracies of the estimated whole-body angular momentum, total mechanical energy and its rate of change were studied through trials of rigid bodies 1–4, by evaluating the conservation of the estimated angular momentum both in magnitude and direction, the conservation of the estimated

total mechanical energy, and errors between the estimated rate of change of the total mechanical energy and zero, respectively. The conservation of the estimated angular momentum in magnitude was analyzed by the relative IQR of the modulus of the estimated whole-body angular momentum, $rL_{\mathrm{IQR}}(\%)$, which was normalized by the median value. The angles between the estimated whole-body angular momentum vector and the X, Y, and Z axes of the inertial triad were calculated, then the IQRs of these angles ($\theta_{\mathrm{IQR},X}$, $\theta_{\mathrm{IQR},Y}$, $\theta_{\mathrm{IQR},Z}$, rad) were analyzed to show the conservation in direction. The IQR was used here instead of standard deviation as a measure of data variability, which could avoid the influence of outliers and nonnormal distribution, and thus ensure reporting robust statistics [35]. The median values of the estimated total mechanical energy were first calculated for every trial of each rigid body. The accuracy of the estimated total mechanical energy was analyzed by calculating the relative IQR of the estimated total mechanical energy $rE_{\mathrm{IQR}}(\%)$, normalized by the median value. Subsequently, errors between the estimated rate of change of the total mechanical energy and zero were normalized by the median value of the total mechanical energy, then its root mean square (rms) values $r\mathrm{d}E/\mathrm{d}t(\%)$ were used for analysis of the accuracy of the estimated rate of change of the total mechanical energy. The lower rL_{IQR}, $\theta_{\mathrm{IQR},X}$, $\theta_{\mathrm{IQR},Y}$, $\theta_{\mathrm{IQR},Z}$, rE_{IQR}, and $r\mathrm{d}E/\mathrm{d}t$ were, the better the estimated angular momentum, total mechanical energy and its rate of change obeyed the conservation laws, which indicated higher estimation accuracies.

3) Evaluation Metrics Based on Internal Action/Reaction Laws: Finally, the accuracies of the estimated action/reaction forces and moments, and power exchange between the two parts of the rigid body, each with its own IMU attached, were studied throughout trials of four rigid bodies, by comparing them both in magnitude and direction. It is noted that since some cylinders were taken away from rigid body 4, all trials of that rigid body were not used for internal action/reaction analysis. Estimation errors in magnitude for these quantities were represented as $\|{}^{\mathcal{N}}\boldsymbol{f}_{\mathrm{act}}(t)\|-\|{}^{\mathcal{N}}\boldsymbol{f}_{\mathrm{react}}(t)\|$, $\|{}^{\mathcal{B}}\boldsymbol{M}_{\mathrm{act}}(t)\| - \|{}^{\mathcal{B}}\boldsymbol{M}_{\mathrm{react}}(t)\|$, and $P_1(t) + P_2(t)$, and they were analyzed by relative rms errors [rF, rM, and rP (%)] normalized by $(\|{}^{\mathcal{N}}\boldsymbol{f}_{\mathrm{act}}(t)\| + \|{}^{\mathcal{N}}\boldsymbol{f}_{\mathrm{react}}(t)\|)/2$, $(\|{}^{\mathcal{B}}\boldsymbol{M}_{\mathrm{act}}(t)\| + \|{}^{\mathcal{B}}\boldsymbol{M}_{\mathrm{react}}(t)\|)/2$, and $(|P_1(t)| + |P_2(t)|)/2$, respectively. Their correlation coefficients [ρF, ρM, and ρP] were then required to assess their opposite direction relationship. Since action/reaction forces and moments were vectors with 3-D, the traditional correlation formulas for comparing two 1-D curves were extended to simultaneously compare the waveforms from all three axes following the method in [36] (the calculation of ρF is shown as the example)

$$\rho F = \frac{\sum_{j=1}^{3}\left[\sum_{t=1}^{n}\left({}^{\mathcal{N}}\boldsymbol{f}_{\mathrm{act},j}(t)-{}^{\mathcal{N}}\bar{\boldsymbol{f}}_{\mathrm{act},j}\right)\left({}^{\mathcal{N}}\boldsymbol{f}_{\mathrm{react},j}(t)-{}^{\mathcal{N}}\bar{\boldsymbol{f}}_{\mathrm{react},j}\right)\right]}{\sum_{j=1}^{3}\sqrt{\sum_{t=1}^{n}\left({}^{\mathcal{N}}\boldsymbol{f}_{\mathrm{act},j}(t)-{}^{\mathcal{N}}\bar{\boldsymbol{f}}_{\mathrm{act},j}\right)^2\sum_{i=1}^{n}\left({}^{\mathcal{N}}\boldsymbol{f}_{\mathrm{react},j}(t)-{}^{\mathcal{N}}\bar{\boldsymbol{f}}_{\mathrm{react},j}\right)^2}} \tag{26}$$

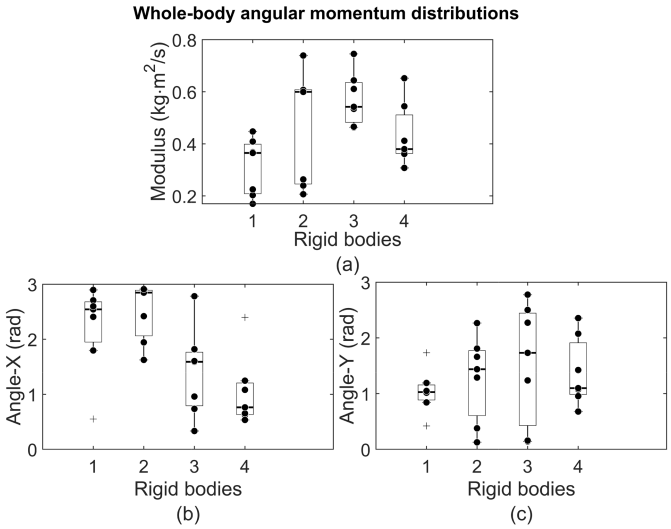

Fig. 5. (a) Distributions of the median values of the modulus and (b) and (c) angles between the estimated whole-body angular momentum and X, Y, and Z axes of the inertial triad over seven trials of each body, in terms of minimum, first quartile, median, third quartile, and maximum.

where $j = 1, 2, 3$ represents the three axes, n is the length of action/reaction forces, and ${}^{\mathcal{N}}\bar{\boldsymbol{f}}_{\mathrm{act},j}$ and ${}^{\mathcal{N}}\bar{\boldsymbol{f}}_{\mathrm{react},j}$ are the mean values of action/reaction forces in each axis. ρM was calculated by the same method. It should be noted that higher accuracy in estimating action/reaction forces and moments, and power exchange between two parts of the rigid body meant smaller rF, rM, and rP, and larger correlation coefficients (ρF, ρM, and ρP).

IV. Results

Fig. 4 shows an example of the original measurements (after sensor calibration and before filtering) expressed in the three axes of the sensor triad of the two IMUs, which were taken from a trial of rigid body 1 with a symmetrical structure and a small mass. Fig. 5 displays the distributions of the median values of the modulus and angles between the estimated whole-body angular momentum and X/Y axes of the inertial triad over seven trials of each rigid body. Figs. 6–9 used the same trial as the example. It should be noted that the original measurements of the two IMUs were very different from each other. By applying the proposed IMU-based estimation methods, we estimated and compared the angular momentum, kinetic, and energetic quantities from these measurements.

A. Angular Momentum Conditions

Fig. 5 shows that how that the IQRs (or Max-min ranges) of the median values of the modulus of the estimated whole-body angular momentum for each rigid body were [58.3% (77.8%), 61.7% (88.3%), 31.5% (53.7%), and 47.4% (89.5%)] compared to their median values, and those for the angles between the estimated whole-body angular momentum and X/Y axes of the inertial triad were [35.8% (92.2%), 33.3% (45.2%), 68.1% (154.1%), and 82.6% (244.0%)] and [34.1% (127.7%), 99.5% (148.8%), 135.4% (152.2%), and 101.9% (152.6%)], respectively. These adequately large IQRs and Max-min ranges demonstrated that we validated the analysis of the estimated

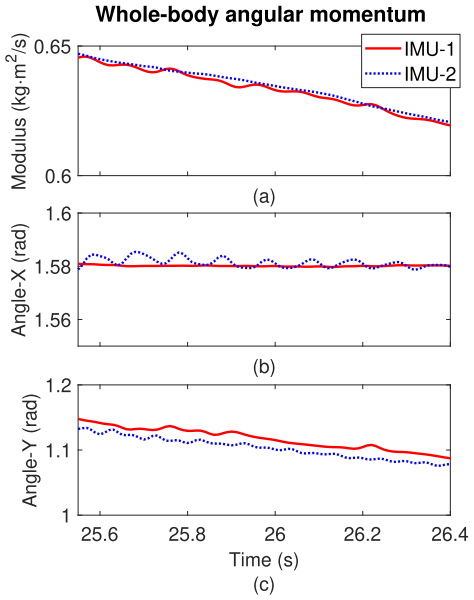

Fig. 6. Example of (a) modulus and (b) and (c) angles between the estimated whole-body angular momentum and X, Y, Z axes of the inertial triad, as a function of time for both IMUs. The same trial as in Fig. 4 is represented. Estimations from IMU-1 and IMU-2 are shown as red-solid and blue-dotted curves, respectively.

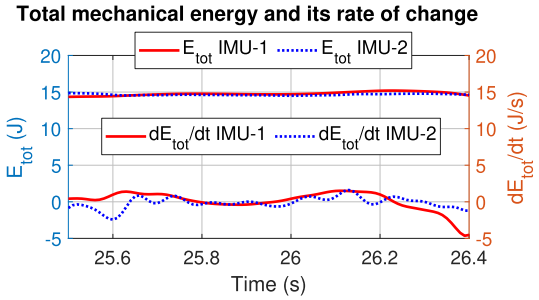

Fig. 7. Estimation results of the total mechanical energy and its rate of change, using the same trial as in Fig. 4. Estimations from IMU-1 and IMU-2 are shown as red-solid and blue-dotted curves, respectively.

TABLE II
EVALUATION OF IMU-BASED ESTIMATION OF THE WHOLE-BODY ANGULAR MOMENTUM, THE TOTAL MECHANICAL ENERGY AND ITS RATE OF CHANGE. RESULTS ARE PRESENTED BY THE (MEAN, STD) OVER ALL TRIALS PER RIGID BODY, AND OVER ALL RIGID BODIES

	rL_{dec} (%)	rL_{IQR} (%)	$\theta_{\mathrm{IQR},X}$ (rad)	$\theta_{\mathrm{IQR},Y}$ (rad)	$\theta_{\mathrm{IQR},Z}$ (rad)	rE_{IQR} (%)	$r\mathrm{d}E/\mathrm{d}t$ (%)
Body 1	(-3.2,0.5)	(0.5,0.3)	(0.03,0.03)	(0.03,0.02)	(0.06,0.04)	(2.5,0.3)	(18.4,7.6)
Body 2	(-2.1,0.6)	(0.2,0.1)	(0.03,0.03)	(0.03,0.03)	(0.06,0.06)	(0.9,0.3)	(8.0,1.3)
Body 3	(-2.2,1.1)	(0.3,0.1)	(0.11,0.12)	(0.05,0.06)	(0.13,0.06)	(1.4,0.7)	(11.1,4.7)
Body 4	(-3.4,1.2)	(0.6,0.2)	(0.16,0.18)	(0.15,0.05)	(0.16,0.06)	(2.5,0.4)	(15.6,4.3)
All bodies	(-2.7,0.7)	(0.4,0.2)	(0.08,0.15)	(0.07,0.06)	(0.10,0.05)	(1.8,0.8)	(13.3,4.6)

angular momentum, kinetic, and energetic quantities against the physical conservation or internal action/reaction laws under adequately varying angular momentum conditions.

B. Validation Results Based on Conservation Laws

The validation results of the estimated whole-body angular momentum are shown in Table II. Presented results are the means and standard deviations (mean, std) of the validation metrics over all trials per rigid body, and the (mean, std) over all rigid bodies. Using the same example as in Fig. 4, the modulus and angles between the estimated whole-body angular momentum and X, Y, and Z axes of the inertial triad are displayed in Fig. 6. During the analysis of results, we observed that the magnitude of the estimated whole-body angular momentum decreased linearly over time as shown in Fig. 6, which could be caused by the air resistance. Therefore, we first extracted this decrease in the angular momentum during the airborne phase from the estimated whole-body angular momentum, which was normalized by the median value, that is, rL_{dec}. The decrease in the modulus of the estimated angular momentum was derived by linear regression. Data variability rL_{IQR} was determined after compensating for this linear decrease with time. The resulting rL_{IQR} was assumed to represent the estimation-induced errors.

Table II shows that decrease in the angular momentum, IQRs of the modulus and angles across all rigid bodies were $(-2.7, 0.7)\%$, $(0.4, 0.2)\%$, $(0.08, 0.15)$ rad, $(0.07, 0.06)$ rad, and $(0.10, 0.05)$ rad, respectively. Compared to rigid body 2 with a large mass and a symmetrical structure, rL_{IQR} of rigid body 1 with a smaller mass but also symmetrical structure, was larger, and rL_{IQR} of rigid body 3, with similar mass but a nonsymmetrical structure, was slightly larger. For rigid body 4, having a small mass and a nonsymmetrical structure, rL_{IQR}, $\theta_{\mathrm{IQR},X}$, $\theta_{\mathrm{IQR},Y}$, and $\theta_{\mathrm{IQR},Z}$ were the largest. The decrease in the relative angular momentum rL_{dec} appeared to be smaller for rigid bodies with larger masses (see the results of rigid bodies 2 and 3).

In Fig. 7, the estimated total mechanical energy and its rate of change of the same example as in Fig. 4 are shown. Results in Table II show that the two estimated quantities had average rE_{IQR} and $r\mathrm{d}E/\mathrm{d}t$ of $(1.8, 0.8)\%$ and $(13.3, 4.6)\%$, respectively, across all rigid bodies, and the rigid body with the smallest mass had the largest rE_{IQR} and $r\mathrm{d}E/\mathrm{d}t$.

C. Validation Results Based on Internal Action/Reaction Laws

Figs. 8 and 9 display the estimated action/reaction forces and moments, and the power exchange between the two parts of the rigid body, using the same trail of rigid body 1 as in Fig. 4. The two parts were divided by the division method 1. Table III summarizes the magnitude [rF, rM, and rP (%)] and directional (ρF, ρM, and ρP) differences in estimating the action/reaction forces and moments, and the power exchange between two parts. The relative magnitude differences for these action/reaction quantities were found to be, on average, $(9.1, 1.9)\%$, $(17.0, 1.9)\%$, and $(19.4, 6.6)\%$, respectively, over all trials and division methods. Their average directional differences in the correlation coefficients were found to be $(-0.89, 0.12)$, $(-0.31, 0.20)$, and $(-0.74, 0.2)$.

Using different division methods, the ratio of the masses of the two parts became larger from the division method 1 to the division method 3, which could be concluded from the division methods mentioned in Section III-C. We can conclude from Table III and the division methods mentioned in Section III-C that when this ratio became larger (from the division method 1 to the division method 3), the accuracies of the estimated

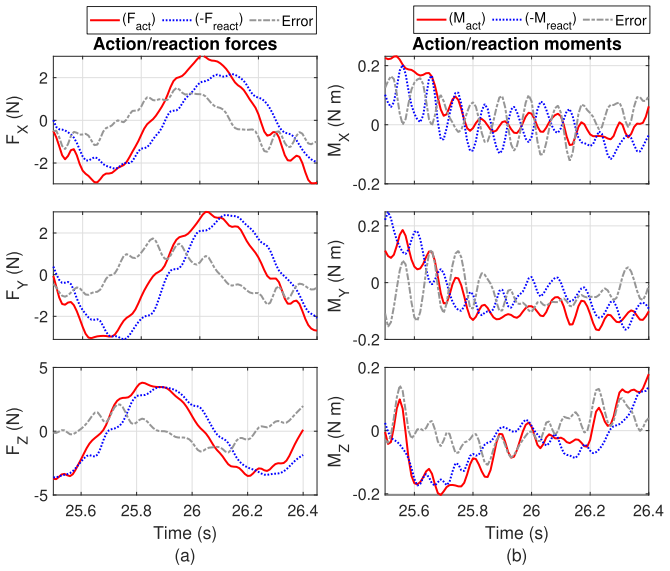

Fig. 8. Kinetics estimation results using the same trial as in Fig. 4. (a) Action/reaction forces between two parts. (b) Action/reaction moments between two parts. The two parts were divided by division method 1. Estimations from two parts in three axes of the body triad are shown as red-solid and blue-dotted curves, respectively, and the gray-dash-dotted curve is the estimation error.

TABLE III
COMPARISON OF IMU-BASED ESTIMATIONS OF THE ACTION/REACTION FORCES, MOMENTS AND POWER EXCHANGE BETWEEN TWO PARTS OF THE RIGID BODY, INCLUDING RELATIVE RMS ERRORS [*rF*, *rM*, AND *rP* (%)], AND THEIR CORRELATION COEFFICIENTS (ρF, ρM, AND ρP). THE LABELS FOR THE THREE DIVISION METHODS ARE 1, 2, AND 3. RESULTS ARE PRESENTED BY THE (MEAN, STD) OVER ALL TRIALS PER RIGID BODY, AND OVER ALL RIGID BODIES

	rF (%)			ρF		
	1	2	3	1	2	3
Body 1	(10.4,3.6)	(6.8,2.7)	(6.2,1.6)	(-0.65,0.34)	(-0.94,0.08)	(-0.94,0.1)
Body 2	(9.0,5.7)	(6.4,4.9)	(5.5,4.3)	(-0.81,0.18)	(-0.98,0.02)	(-0.99,0.01)
Body 3	(14.4,1.9)	(12.1,2.9)	(11.4,1.5)	(-0.83,0.07)	(-0.96,0.02)	(-0.95,0.02)
All bodies	(11.3,2.8)	(8.4,3.2)	(7.7,3.2)	(-0.76,0.1)	(-0.96,0.02)	(-0.96,0.03)
	rM (%)			ρM		
	1	2	3	1	2	3
Body 1	(16.1,4.1)	(20.9,4.9)	(17.8,5.0)	(-0.25,0.49)	(-0.06,0.5)	(0.01,0.35)
Body 2	(16.5,5.4)	(15.8,9.5)	(16.3,2.5)	(-0.6,0.25)	(-0.61,0.24)	(-0.31,0.13)
Body 3	(12.8,7.5)	(13.7,7.3)	(22.7,6.1)	(-0.55,0.32)	(-0.44,0.35)	(0.03,0.22)
All bodies	(15.1,2.0)	(16.8,3.7)	(18.9,3.0)	(-0.47,0.19)	(-0.37,0.28)	(-0.09,0.19)
	rP (%)			ρP		
	1	2	3	1	2	3
Body 1	(26.2,8.8)	(15.8,2.3)	(13.3,3.9)	(-0.58,0.44)	(-0.69,0.19)	(-0.94,0.08)
Body 2	(24.8,8.1)	(12.9,2.1)	(12.6,4.5)	(-0.64,0.39)	(-0.97,0.03)	(-0.97,0.03)
Body 3	(28.6,4.1)	(26.2,1.4)	(14.4,1.6)	(-0.39,0.37)	(-0.52,0.22)	(-0.96,0.02)
All bodies	(26.4,1.9)	(18.4,7.1)	(13.4,0.9)	(-0.54,0.13)	(-0.73,0.2)	(-0.96,0.02)

action/reaction forces and power exchange between the two parts showed a trend to be higher, that is, rF and rP decreased, ρF and ρP increased. In contrary, the accuracy of the estimated action/reaction moments between the two parts became lower, with increasing rM and decreasing ρM.

V. DISCUSSION

A. Use of Physical Laws for Evaluation of Estimates of Kinetic and Energetic Quantities

The accuracies of the estimated whole-body angular momentum, and total mechanical energy and its rate of change were evaluated based on the conservation laws of the angular momentum and the total mechanical energy during ballistic motions, and the accuracies of the kinetics and power exchange were validated by analyzing the estimated internal action/reaction forces and moments of and power exchange between the two parts of the rigid body, each with a separate IMU. This allowed us to circumvent the limitations of using optical MOCAP systems as [12], [13], that is, avoiding inheriting the inaccuracies of optical MOCAP systems in measuring the required kinematics due to differentiations. It further avoided repeatedly evaluating only the kinematics in the kinetic and energetic levels, since the same mass and inertia tensors were applied in both IMU-based and optical MOCAP-based kinetic and energetic estimates. Moreover, using physical laws can avoid the experimental setup complexity of using force/moment sensors [20], [37].

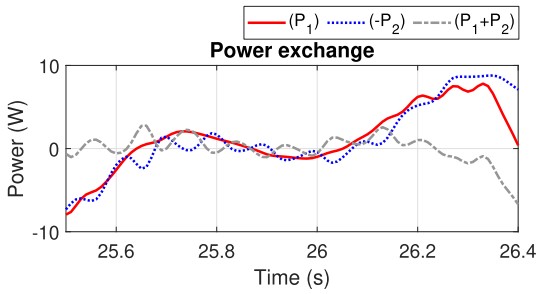

Fig. 9. Estimation results of the power exchange between two parts of the rigid body, using the same trial as in Fig. 4. The two parts were divided by division method 1. Estimations of the power exchange of these two parts based on the signals from their own IMUs, and their error are shown as red-solid, blue-dotted, and gray-dash-dotted curves, respectively.

B. Multiple Sources of Errors

The errors in the estimated quantities were caused by several reasons. The errors in original IMU signals due to their limited precision or uncalibrated errors such as **g**-sensitivity and $\mathbf{g}^2$-sensitivity [38] may represent large errors in dynamic motions. Moreover, the uncertainties of rigid body parameters and vibrations in the carbon tubes due to their inadequate rigidity also introduced additional estimation errors. The above reasons for the estimation errors will be analyzed in detail.

1) Errors in Original IMU Signals: Errors in original IMU signals significantly impact the accuracy of estimated quantities, as evident from the angular momentum, kinetic, and energetic definitions in Section III-A. Precision in angular velocity measurements is pivotal, as errors therein affect the estimated quantities in various ways. These errors directly impact quantities dependent on angular velocity and subsequently introduce inaccuracies in quantities reliant on angular acceleration, computed via differentiating the angular velocity. Furthermore, the rotation matrix between the body and inertial triads accumulates errors since it was estimated by integrating the angular velocity measurements. This can induce errors wherever the rotation matrix is applied, such as in rotating the gravity acceleration expressed in the inertial triad to the body triad, transferring the estimated whole-body angular momentum from the body triad to the inertial triad, etc. Therefore, precise gyroscope measurements during ballistic

TABLE IV
COMPARISON OF ANGULAR VELOCITY MEASUREMENTS, INCLUDING THE RELATIVE IQR OF THE MODULUS OF THE ANGULAR VELOCITY MEASUREMENTS ($r\omega_{\mathrm{IQR}}$, %), AND OFFSETS OF THE ANGULAR VELOCITY MEASUREMENTS BEFORE AND AFTER MEASUREMENT ($\mathrm{offset}_{\mathrm{pri}}$ AND $\mathrm{offset}_{\mathrm{post}}$, rad/s). RESULTS ARE PRESENTED BY THE (MEAN, STD) OVER ALL TRIALS PER RIGID BODY

	$r\omega_{\mathrm{IQR}}$ (%)	$\mathrm{offset}_{\mathrm{pri}}$ (rad/s)	$\mathrm{offset}_{\mathrm{post}}$ (rad/s)
Body 1	(3.6,0.9)	$(0.19,0.01)\times10^{-2}$	$(0.13,0.05)\times10^{-2}$
Body 2	(2.0,0.3)	$(0.19,0.01)\times10^{-2}$	$(0.14,0.02)\times10^{-2}$
Body 3	(3.2,3.6)	$(0.19,0.00)\times10^{-2}$	$(0.14,0.03)\times10^{-2}$
Body 4	(4.7,2.7)	$(0.19,0.01)\times10^{-2}$	$(0.14,0.03)\times10^{-2}$

TABLE V
DIFFERENCES OF ANGULAR VELOCITIES AND ANGULAR ACCELERATIONS (EXPRESSED IN THE BODY TRIAD) FROM TWO IMUS, INCLUDING THE RELATIVE RMS DIFFERENCES BETWEEN THE MODULUS (ω_{mag} AND α_{mag}, %) OF THE ANGULAR VELOCITIES AND ANGULAR ACCELERATIONS FROM TWO IMUS, WHICH WERE NORMALIZED BY THE AVERAGE VALUE OF THEIR MEDIANS, AND THE RMS DIFFERENCES OF THEIR ANGLE DIFFERENCES (ω_{dir} AND α_{dir}, rad). RESULTS ARE PRESENTED BY THE (MEAN, STD) OVER ALL TRIALS PER RIGID BODY

	ω_{mag} (%)	α_{mag} (%)	ω_{dir} (rad)	α_{dir} (rad)
Body 1	(0.5,0.4)	(12.3,3.2)	(0.09,0.07)	(0.30,0.25)
Body 2	(0.2,0.1)	(13.9,3.0)	(0.09,0.07)	(0.30,0.27)
Body 3	(1.0,0.5)	(13.1,9.2)	(0.12,0.01)	(0.16,0.08)

All the trials of rigid body 4 were not used for internal action/reaction analysis, thus rigid body 4 was not included in this table.

motion are very important. We enhanced angular velocity measurement precision through gyroscope recalibration, correcting misalignment matrices, scale factors, and zero offsets, following [33].

Table IV compares the precision of the angular velocity measurements from the level of the whole rigid body. According to the conservation law of the whole-body angular momentum during airborne phases, the modulus of the angular velocity measurements should also keep constant. Table IV presents comparisons using relative IQR ($r\omega_{\mathrm{IQR}}$, %) of the angular velocity modulus normalized by median values and offsets of angular velocity measurements before and after measurement (offsetpri and offsetpost, rad/s). The modulus of angular velocity measurements is defined as

$$\left|{}^{\mathcal{F}}\boldsymbol{\omega}_s(t)\right| = \sqrt{{}^{\mathcal{F}}\boldsymbol{\omega}_{s,x}(t)^2 + {}^{\mathcal{F}}\boldsymbol{\omega}_{s,y}(t)^2 + {}^{\mathcal{F}}\boldsymbol{\omega}_{s,z}(t)^2}. \quad (27)$$

Differences in angular velocity offsets before and after measurement remained consistent across all trials, with a minimal 0.05×10^{-2} rad/s increase post-measurement, signifying negligible changes over time. These offsets were not the main reason leading to the remarkable difference in the estimated whole-body angular momentum, total mechanical energy, and its rate of change. Given the dynamic and complex nature of ballistic motions, the $\mathbf{g}$-sensitivity and $\mathbf{g}^2$-sensitivity [38] of the gyroscope due to linear acceleration and vibrations may represent the largest error source, which were not compensated in this article and could lead to large errors in the angular velocity measurements and subsequently, in other estimated quantities.

Internal action/reaction kinetics and power exchange between two parts of the rigid body were estimated using separate IMU measurements. Differences in kinematic estimations between these IMUs yielded variations in these estimated quantities. Table V illustrates the differences in angular velocities and accelerations between the two IMUs, presented in the body triad. Magnitude differences were calculated as relative rms differences between angular velocity and acceleration moduli from the two IMUs, normalized by the average value of their medians. Directional differences were assessed through rms differences in their angles. Ideally, both differences should be zero. However, Table V reveals large angular acceleration differences, indicating that variations in angular velocity measurements led to even larger differences in angular acceleration post-differentiation. These differences, particularly in the angular acceleration, likely contribute to estimation errors in the internal action/reaction kinetics and power exchange between two parts of the rigid body from the perspective of measurement errors in signals.

2) Errors Induced by Uncertainties in the Rigid Body: Errors in original IMU signals may not completely explain the errors in the estimated quantities. Quantitative analysis of the influence of the variability in estimating human body segment inertial parameters for accurate inverse dynamics analyses of gait was studied in the literature [39], [40]. They pointed out that the errors in the inertial parameters of the human body segments were not the main source of errors but still cannot be ignored. Potential errors in the calculated CoM, the total mass, and inertia tensor of the rigid bodies constructed for the current study arose from various factors. These included ignoring the mass of light carbon tubes, approximating the middle Aluminum disk as a solid cylinder despite six screw holes for tube fixation, and potential assembly and alignment errors between hollow cylinders. These uncertainties introduced additional errors in determining rigid body parameters, particularly for structures with nonsymmetrical designs and lower mass. Consequently, such uncertainties could amplify errors in estimating angular momentum, kinetics, and energetics.

Results in Table III indicate that the estimated action/reaction moments exhibited lower correlation coefficients (-0.32, 0.20) across all rigid bodies and division methods compared to the estimated action/reaction forces and power exchange. Despite the errors in the IMU measurements and rigid body parameters, another possible error could be the uncertainty in the location of the contact point. Although we assumed the contact point between the two parts to be at the center disc's midpoint, practical determination of this point is challenging. Given the small magnitude of action/reaction moments in our experiments [see Fig. 8(b)], an offset in moment arms of action/reaction forces could compound more errors in estimated action/reaction moments.

3) Errors Due to the Contradiction of the Initial Assumption of Rigid Body: Our results rested on the assumption of

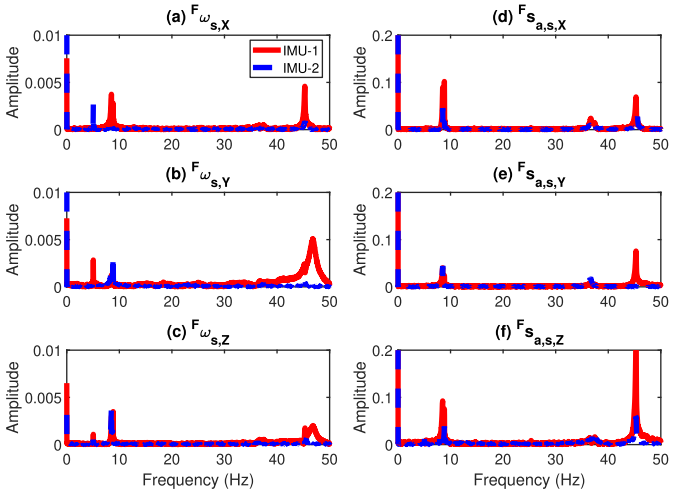

Fig. 10. Frequency analysis results of the oscillation test, (a) gyroscope measurements and (b) accelerometer measurements. Results from IMU-1 and IMU-2 are shown as red-solid and blue-dotted curves, respectively.

high strength and rigidity in the carbon tubes, rendering our self-designed structure a rigid body. However, as evident in Figs. 4, 6, 8, and 9, unexpected oscillations affected both original measurements and estimation outcomes. We hypothesized these oscillations stemmed from vibrations in the carbon tubes, attributable to their inadequate strength and rigidity. To verify the hypothesis, we fixated the rigid body on a stable table and manually excited one of the tubes with a random certain force. Frequency analysis of IMU measurements using fast Fourier transform (FFT) in Fig. 10 showed two primary components at approximately 10 and 45 Hz. Although the higher frequency component could be removed by our filtering progress, the lower frequency component persisted, introducing additional errors to our estimations. These findings indicated insufficient strength and rigidity of the carbon tubes, which contradicted our initial assumption of a rigid body. Notably, errors linked to carbon tube vibrations in estimated quantities depend on the quantity's magnitude and vibration amplitude. For instance, in Fig. 8(b), oscillations exerted a larger influence on action/reaction moment estimates than on action/reaction forces estimates due to a higher ratio of desired estimation to oscillations for the action/reaction moments.

C. Limitations and Future Work

The presented evaluation method using physical laws during ballistic motions also has limitations that need to be considered in addition to the advantages that it circumvents the use of optical MOCAP systems and simplifies the experimental setup. Evaluation based on physical laws only provided a partial validation of the IMU-based estimates of the quantities, and the evaluation with absolute references was not conducted. However, this partial validation is still very important and interesting and provides a potential evaluation solution without using external measurement devices. Furthermore, because of the lack of an accurate reference of the kinematics, the quantitative analysis of the sensitivity of the IMU-based estimation methods to the errors in rigid body parameters could not be performed in this article. In the future, with more accurate IMU measurements, a more detailed quantitative sensitivity analysis should be conducted by, for example, re-calculating the CoM by minimizing the sum squared error between action/reaction forces [20], or re-calculating the inertia tensor by minimizing the estimated net external moment during ballistic motions.

In this article, the $\mathbf{g}$-sensitivity and $\mathbf{g}^2$-sensitivity of the gyroscope due to linear acceleration and vibrations were not calibrated, and these two sensitivities may represent a substantial error source, which may lead to considerable errors in our estimation results. Therefore, it is important that IMUs are calibrated well to reduce measurement errors induced by $\mathbf{g}$-sensitivity and $\mathbf{g}^2$-sensitivity [38], [41]. Advanced kinematics estimation methods [42], [43] should also be considered to improve the accuracy of kinematics estimations. For example, in applications of human movements, interactions with the environment in many cases have a cyclical nature. Thus, prior information about the movements can be taken into account to improve the estimation accuracy. For example, our previous work proposed a drift-free 3-D orientation and displacement estimation using one IMU based on the assumption of an approximately constant cycle average velocity in quasi-cyclical movements [44].

The movements evaluated in our experiments had a relatively short duration of 1 s for throwing experiments. The estimation error is expected to increase for longer-lasting movements, due to integration errors. Therefore, a similar experiment shown in this study with a longer free fall duration should be performed as a follow-up. Moreover, as a further application, similar free motion experiments in the air with human subjects may be done to validate the proposed method in real applications, such as when people do sports like the high jump, long jump or interaction scenarios like volleyball players jump and hit the ball [45].

Zero-phase low-pass and high-pass filters were used to reduce noise, and forward/backward Kalman filter-based smoother [46] was used to reduce drift in orientation, velocity and position estimations. However, they can be only conducted in offline data processing, which is also a limitation of our work. In future real-time applications of our work, the phase delay due to filtering should be considered.

VI. Conclusion

In this article, we introduced an IMU-based method for estimating angular momentum, kinetics, and energetics, including the total mechanical energy and its rate of change, of a single rigid body. To eliminate the need for using optical MOCAP systems as a reference during evaluation, we proposed an innovative validation approach. This method assessed the IMU-based estimation by leveraging physical conservation and action/reaction laws during free ballistic motions, avoiding the dependence on external reference measurement devices like F&M sensors or optical MOCAP systems.

The evaluation results demonstrated that we could estimate these quantities of a rigid body by only using angular velocity and acceleration signals supplied by an IMU. By utilizing our evaluation method, we avoid inaccuracies arising from

differentiation errors in optical marker data for kinematics and the repetition of kinematic evaluations due to using identical mass and inertia tensors in both IMU-based and optical MOCAP-based kinetic and energetic assessments. However, the evaluation results highlighted that the accuracy of this method was sensitive to the differences in both original IMU measurements under dynamic conditions, especially concerning angular velocity. The uncertainties in calculating rigid body parameters (i.e., the CoM, total mass or inertia tensor) also cannot be ignored. Additionally, we found that vibrations in the carbon tubes due to their insufficient strength and rigidity had a non-negligible impact on estimation accuracy, and can be dominant when the amplitude of vibrations was comparable to the estimated quantity. These limitations aside, the work of this article may be useful in daily life conditions for portably analyzing the kinetics, angular momentum, and energetic quantities of humans such as in sports applications, physical labor, and rehabilitation.

APPENDIX
ESTIMATION OF ORIENTATION, ACCELERATION, VELOCITY AND POSITION OF THE COM

A. Orientation Estimation

An Error-state Kalman Filter (ESKF) modified from [47], was used to estimate the orientation ${}^{\mathcal{N}}\boldsymbol{C}_{\mathcal{B}}(t)$. The measurement update step of the original ESKF assumed that the total acceleration measured by the accelerometer contains low free acceleration. However, accelerometer measurements under dynamic conditions in which we studied the kinematics of the rigid body included large free accelerations. Assuming that these dynamic conditions occurred during periods of limited duration, the accelerometer measurement was only applied if the norm of the gyroscope signal was below a threshold of 2.5°/s, assuming this indicated a static condition. The applied threshold was determined by trial and error. Under nonstatic conditions, the orientation was only estimated by integrating the gyroscope signals. The drift error of orientation estimations increased continuously over time using the ESKF, which is a forward filter, a backward filter was then engaged and the last orientation estimate was propagated back in time. A smoother [46] was added to reduce the orientation estimation error post-hoc by fusing estimates from both forward and backward, which was weighted by the covariances of forward and backward estimates.

B. CoM Acceleration Estimation

In (4), the acceleration of the CoM ${}^{\mathcal{N}}\boldsymbol{a}_C(t)$ is calculated from the acceleration two point theorem of the rigid body [34] as

$$\begin{aligned}{}^{\mathcal{N}}\boldsymbol{a}_C(t) = {}&{}^{\mathcal{N}}\boldsymbol{a}_s(t) + {}^{\mathcal{N}}\boldsymbol{C}_{\mathcal{B}}(t)\left({}^{\mathcal{B}}\boldsymbol{\alpha}_b(t) \times {}^{\mathcal{B}}\boldsymbol{r}_{C/S}\right)\\ &+ {}^{\mathcal{N}}\boldsymbol{C}_{\mathcal{B}}(t)\left[{}^{\mathcal{B}}\boldsymbol{\omega}_b(t) \times \left({}^{\mathcal{B}}\boldsymbol{\omega}_b(t) \times {}^{\mathcal{B}}\boldsymbol{r}_{C/S}\right)\right] \quad (28)\end{aligned}$$

where ${}^{\mathcal{B}}\boldsymbol{\alpha}_b(t)$ is the angular acceleration of the rigid body which has been defined in (3). In terms of the original signals of IMU, (27) can be expressed as

$$\begin{aligned}{}^{\mathcal{N}}\boldsymbol{a}_C(t) = {}&{}^{\mathcal{N}}\boldsymbol{C}_{\mathcal{B}}(t){}^{\mathcal{B}}\boldsymbol{C}_{\mathcal{F}}\left[{}^{\mathcal{F}}\boldsymbol{s}_{a,s}(t) + {}^{\mathcal{F}}\dot{\boldsymbol{\omega}}_s(t) \times {}^{\mathcal{F}}\boldsymbol{r}_{C/S} + {}^{\mathcal{F}}\boldsymbol{\omega}_s(t)\right.\\ &\left.\times \left({}^{\mathcal{F}}\boldsymbol{\omega}_s(t) \times {}^{\mathcal{F}}\boldsymbol{r}_{C/S}\right)\right] + {}^{\mathcal{N}}\boldsymbol{g}. \quad (29)\end{aligned}$$

C. CoM Position and Velocity Estimation

The estimation of the acceleration of the CoM was introduced in Appendix B, then, the velocity was estimated by the zero velocity update (ZUPT)-based velocity estimation method introduced below. The discrete model for velocity estimation was expressed by

$${}^{\mathcal{N}}\boldsymbol{v}_C(t+\Delta t) = {}^{\mathcal{N}}\boldsymbol{v}_C(t) + {}^{\mathcal{N}}\boldsymbol{a}_C(t)\Delta t. \quad (30)$$

Instead of direct integration of the acceleration, a ZUPT-based Kalman filter was used to reduce the drift in velocity estimation. At the beginning and end of each experimental trial, the velocity of the rigid body was kept zero. A post-hoc smoother, similar to the smoother applied for the orientation estimation, was also added to reduce the estimation error. The estimated CoM velocity was then integrated to calculate the CoM position ${}^{\mathcal{N}}\boldsymbol{r}_C(t)$ as

$${}^{\mathcal{N}}\boldsymbol{r}_C(t+\Delta t) = {}^{\mathcal{N}}\boldsymbol{r}_C(t) + {}^{\mathcal{N}}\boldsymbol{v}_C(t)\Delta t. \quad (31)$$

Similar zero velocity condition and smoother were also used in the CoM position estimation.

ACKNOWLEDGMENT

The authors would like to thank Leendert Schaake, Roessingh Research and Development, Enschede, The Netherlands, for assisting with the measurement setups, and E. H. F. van Asseldonk, University of Twente, Enschede, for the improvement of the article.

REFERENCES

[1] R. van Middelaar, P. Veltink, and J. Reenalda, "Modeling the total force at the knee joint during a fatiguing run: 56," *Med. Sci. Sports Exercise*, vol. 54, no. 9S, p. 5, 2022.
[2] X. Zhang, R. Xia, B. Dai, X. Sun, and W. Fu, "Effects of exercise-induced fatigue on lower extremity joint mechanics, stiffness, and energy absorption during landings," *J. Sports Sci. Med.*, vol. 17, no. 4, pp. 640–649, 2018.
[3] M. van Mierlo, J. I. Ambrosius, M. Vlutters, E. H. F. van Asseldonk, and H. van der Kooij, "Recovery from sagittal-plane whole body angular momentum perturbations during walking," *J. Biomech.*, vol. 141, Aug. 2022, Art. no. 111169.
[4] C. Bayón et al., "Can momentum-based control predict human balance recovery strategies?" *IEEE Trans. Neural Syst. Rehabil. Eng.*, vol. 28, no. 9, pp. 2015–2024, Sep. 2020.
[5] S. T. Orange, J. W. Metcalfe, A. Liefeith, and A. R. Jordan, "Validity of various portable devices to measure sit-to-stand velocity and power in older adults," *Gait Posture*, vol. 76, pp. 409–414, Feb. 2020.
[6] K. Hashimoto et al., "Biped walking stabilization based on gait analysis," in *Proc. IEEE Int. Conf. Robot. Autom.*, May 2012, pp. 154–159.
[7] D. A. Winter, *Biomechanics Motor Control Human Movement*. Hoboken, NJ, USA: Wiley, 2009.
[8] D. Roetenberg, H. J. Luinge, C. T. M. Baten, and P. H. Veltink, "Compensation of magnetic disturbances improves inertial and magnetic sensing of human body segment orientation," *IEEE Trans. Neural Syst. Rehabil. Eng.*, vol. 13, no. 3, pp. 395–405, Sep. 2005.
[9] D. Roetenberg, C. T. M. Baten, and P. H. Veltink, "Estimating body segment orientation by applying inertial and magnetic sensing near ferromagnetic materials," *IEEE Trans. Neural Syst. Rehabil. Eng.*, vol. 15, no. 3, pp. 469–471, Sep. 2007.
[10] M. I. M. Refai, B. F. van Beijnum, J. H. Buurke, and P. H. Veltink, "Portable gait lab: Tracking relative distances of feet and CoM using three IMUs," *IEEE Trans. Neural Syst. Rehabil. Eng.*, vol. 28, no. 10, pp. 2255–2264, Oct. 2020.
[11] L. Sy et al., "Estimating lower limb kinematics using a reduced wearable sensor count," *IEEE Trans. Biomed. Eng.*, vol. 68, no. 4, pp. 1293–1304, Apr. 2021.

[12] H. Hanawa et al., "Validity of inertial measurement units in assessing segment angles and mechanical energies of elderly persons during sit-to-stand motion," in *Proc. 58th Annu. Conf. Soc. Instrum. Control Eng. Jpn. (SICE)*, Sep. 2019, pp. 936–940.

[13] K. Lepetit et al., "Optimized scoring tool to quantify the functional performance during the sit-to-stand transition with a magneto-inertial measurement unit," *Clin. Biomech.*, vol. 69, pp. 109–114, Oct. 2019.

[14] A. Karatsidis, G. Bellusci, H. Schepers, M. de Zee, M. Andersen, and P. Veltink, "Estimation of ground reaction forces and moments during gait using only inertial motion capture," *Sensors*, vol. 17, no. 12, p. 75, Dec. 2016.

[15] E. C.-Y. Yang and M.-H. Mao, "3D analysis system for estimating intersegmental forces and moments exerted on human lower limbs during walking motion," *Measurement*, vol. 73, pp. 171–179, Sep. 2015.

[16] M. I. M. Refai, B. F. van Beijnum, J. H. Buurke, and P. H. Veltink, "Portable gait lab: Estimating 3D GRF using a pelvis IMU in a foot IMU defined frame," *IEEE Trans. Neural Syst. Rehabil. Eng.*, vol. 28, no. 6, pp. 1308–1316, Jun. 2020.

[17] W. R. Johnson, A. Mian, M. A. Robinson, J. Verheul, D. G. Lloyd, and J. A. Alderson, "Multidimensional ground reaction forces and moments from wearable sensor accelerations via deep learning," *IEEE Trans. Biomed. Eng.*, vol. 68, no. 1, pp. 289–297, Jan. 2021.

[18] F. J. Wouda et al., "Estimation of vertical ground reaction forces and sagittal knee kinematics during running using three inertial sensors," *Frontiers Physiol.*, vol. 9, p. 218, Mar. 2018.

[19] P. H. Veltink, H. Kortier, and H. M. Schepers, "Sensing power transfer between the human body and the environment," *IEEE Trans. Biomed. Eng.*, vol. 56, no. 6, pp. 1711–1718, Jun. 2009.

[20] R. S. McGinnis, J. Hough, and N. C. Perkins, "Accuracy of wearable sensors for estimating joint reactions," *J. Comput. Nonlinear Dyn.*, vol. 12, no. 4, Jul. 2017, Art. no. 041010.

[21] P. H. Veltink, C. Liedtke, E. Droog, and H. van der Kooij, "Ambulatory measurement of ground reaction forces," *IEEE Trans. Neural Syst. Rehabil. Eng.*, vol. 13, no. 3, pp. 423–427, Sep. 2005.

[22] H. M. Schepers, H. F. J. M. Koopman, and P. H. Veltink, "Ambulatory assessment of ankle and foot dynamics," *IEEE Trans. Biomed. Eng.*, vol. 54, no. 5, pp. 895–902, May 2007.

[23] M. I. M. Refai, B. F. van Beijnum, J. H. Buurke, and P. H. Veltink, "Gait and dynamic balance sensing using wearable foot sensors," *IEEE Trans. Neural Syst. Rehabil. Eng.*, vol. 27, no. 2, pp. 218–227, Feb. 2019.

[24] E. Shahabpoor and A. Pavic, "Measurement of walking ground reactions in real-life environments: A systematic review of techniques and technologies," *Sensors*, vol. 17, no. 9, p. 2085, Sep. 2017.

[25] Y. Na and J. Kim, "Dynamic elbow flexion force estimation through a muscle twitch model and sEMG in a fatigue condition," *IEEE Trans. Neural Syst. Rehabil. Eng.*, vol. 25, no. 9, pp. 1431–1439, Sep. 2017.

[26] J. Zhang et al., "Boosting personalized musculoskeletal modeling with physics-informed knowledge transfer," *IEEE Trans. Instrum. Meas.*, vol. 72, pp. 1–11, 2023.

[27] J. Zhang et al., "Physics-informed deep learning for musculoskeletal modeling: Predicting muscle forces and joint kinematics from surface EMG," *IEEE Trans. Neural Syst. Rehabil. Eng.*, vol. 31, pp. 484–493, 2023.

[28] A. J. van den Bogert, L. Read, and B. M. Nigg, "A method for inverse dynamic analysis using accelerometry," *J. Biomech.*, vol. 29, no. 7, pp. 949–954, Jul. 1996.

[29] A. Karatsidis et al., "Musculoskeletal model-based inverse dynamic analysis under ambulatory conditions using inertial motion capture," *Med. Eng. Phys.*, vol. 65, pp. 68–77, Mar. 2019.

[30] M. M. Diraneyya, J. Ryu, E. Abdel-Rahman, and C. T. Haas, "Inertial motion capture-based whole-body inverse dynamics," *Sensors*, vol. 21, no. 21, p. 7353, Nov. 2021.

[31] K. Lepetit, K. Ben Mansour, S. Boudaoud, K. Kinugawa-Bourron, and F. Marin, "Evaluation of the kinetic energy of the torso by magneto-inertial measurement unit during the sit-to-stand movement," *J. Biomechanics*, vol. 67, pp. 172–176, Jan. 2018.

[32] H. Vallery and A. L. Schwab, *Advanced Dynamics*. Delft, The Netherlands: Delft Univ. Technology, 2017.

[33] D. Tedaldi, A. Pretto, and E. Menegatti, "A robust and easy to implement method for IMU calibration without external equipments," in *Proc. IEEE Int. Conf. Robot. Autom. (ICRA)*, May 2014, pp. 3042–3049.

[34] T. R. Kane and D. A. Levinson, *Dynamics, Theory and Applications*. New York, NY, USA: McGraw-Hill, 1985.

[35] Analytical Methods Committee, "Robust statistics-how not to reject outliers—Part 1. basic concepts," *Analyst*, vol. 114, no. 12, pp. 1693–1697, 1989.

[36] B. C. Bennett, S. D. Russell, P. Sheth, and M. F. Abel, "Angular momentum of walking at different speeds," *Human Movement Sci.*, vol. 29, no. 1, pp. 114–124, Feb. 2010.

[37] J. Hough, R. S. McGinnis, and N. C. Perkins, "Benchmarking the accuracy of inertial measurement units for estimating kinetic energy," in *Proc. ASME Int. Mech. Eng. Congr. Expo.*, Nov. 2013, Paper V03BT03A005. [Online]. Available: https://doi.org/10.1115/IMECE2013-63303

[38] X. Zhang et al., "Low-cost inertial measurement unit calibration with nonlinear scale factors," *IEEE Trans. Ind. Informat.*, vol. 18, no. 2, pp. 1028–1038, Feb. 2022.

[39] J. A. Reinbolt, R. T. Haftka, T. L. Chmielewski, and B. J. Fregly, "Are patient-specific joint and inertial parameters necessary for accurate inverse dynamics analyses of gait," *IEEE Trans. Biomed. Eng.*, vol. 54, no. 5, pp. 782–793, May 2007.

[40] J. E. Langenderfer, P. J. Laz, A. J. Petrella, and P. J. Rullkoetter, "An efficient probabilistic methodology for incorporating uncertainty in body segment parameters and anatomical landmarks in joint loadings estimated from inverse dynamics," *J. Biomechanical Eng.*, vol. 130, no. 1, Feb. 2008, Art. no. 014502.

[41] M. Brossard, S. Bonnabel, and A. Barrau, "Denoising IMU gyroscopes with deep learning for open-loop attitude estimation," *IEEE Robot. Autom. Lett.*, vol. 5, no. 3, pp. 4796–4803, Jul. 2020.

[42] J.-H. Zhang, P. Li, C.-C. Jin, W.-A. Zhang, and S. Liu, "A novel adaptive Kalman filtering approach to human motion tracking with magnetic-inertial sensors," *IEEE Trans. Ind. Electron.*, vol. 67, no. 10, pp. 8659–8669, Oct. 2020.

[43] P. Li, W.-A. Zhang, and J.-H. Zhang, "HMM based adaptive Kalman filter for orientation estimation," *IEEE Sensors J.*, vol. 22, no. 17, pp. 17065–17074, Sep. 2022.

[44] M. A. Zandbergen, J. Reenalda, R. P. van Middelaar, R. I. Ferla, J. H. Buurke, and P. H. Veltink, "Drift-free 3D orientation and displacement estimation for quasi-cyclical movements using one inertial measurement unit: Application to running," *Sensors*, vol. 22, no. 3, p. 956, Jan. 2022.

[45] S. Garcia, N. Delattre, E. Berton, G. Divrechy, and G. Rao, "Comparison of landing kinematics and kinetics between experienced and novice volleyball players during block and spike jumps," *BMC Sports Sci., Med. Rehabil.*, vol. 14, no. 1, p. 105, Dec. 2022.

[46] S. I. Roumeliotis, G. S. Sukhatme, and G. A. Bekey, "Smoother based 3D attitude estimation for mobile robot localization," in *Proc. IEEE Int. Conf. Robot. Autom.*, May 1999, pp. 1979–1986.

[47] J. Solà, "Quaternion kinematics for the error-state Kalman filter," 2017, *arXiv:1711.02508*.

Junhao Zhang received the B.Eng. degree in automation and the M.Eng. degree in control science and engineering from the Zhejiang University of Technology, Hangzhou, China, in 2017 and 2020, respectively. He is currently pursuing the Ph.D. degree with the Department of Biomedical Signals and Systems, University of Twente, Enschede, The Netherlands, supported by the China Scholarship Council.

His research interests include biomechanics and human movement analysis based on inertial sensors.

Frodo Muijzer received the B.Sc. and M.Sc. degrees in biomedical engineering from the University of Twente, Enschede, The Netherlands, in 2012 and 2014, respectively.

After graduation, he worked for six years at TMSi, Oldenzaal, The Netherlands, providing technical support to researchers using TMSis EEG and EMG equipment. He worked on the requirements engineering and verification. In 2020, he started as a Technician at the Biomedical Signals and Systems Group, University of Twente. He is responsible for the development of custom sensing hardware used in research and education and for the technical dossiers required when prototype devices are used in a clinical setting.

Heike Vallery (Member, IEEE) received the Dipl.-Ing. degree in mechanical engineering from RWTH Aachen University, Aachen, Germany, in 2004, and the Dr.-Ing. degree from the Technische Universitt Mnchen, Munich, Germany, in 2009.

She continued her academic career at ETH Zürich, Zürich, Switzerland; Khalifa University, Abu Dhabi, United Arab Emirates; and TU Delft, CD Delft, The Netherlands. She is now a Full Professor with RWTH Aachen University and TU Delft, and also holds an Honorary Professorship at Erasmus MC, Rotterdam, The Netherlands. Her main research interests include designs and control of minimalistic robotics.

Peter H. Veltink (Senior Member, IEEE) is a Professor of Technology for the restoration of human function with the University of Twente, Enschede, The Netherlands. He chairs the Biomedical Signals and Systems Group and is the Vice-Dean of research of the Faculty of Electrical Engineering, Mathematics, and Computer Science. His research interest includes ambulatory human movement analysis using inertial sensors, with applications in rehabilitation medicine and biomechanics. He has been the scientific coordinator of three EU research training networks and coordinated the EU-FP7 ICT project INTERACTION and the EU-H2020 ICT project eNHANCE.